Research Square

Preprints are preliminary reports that have not undergone peer review.
They should not be considered conclusive, used to inform clinical practice,
or referenced by the media as validated information.

Spatiotemporal Network Analysis of Actual Evapotranspiration Dynamics and Causal Teleconnections in Iran

Mohammad Kamangar

mohamad.kamangar63@gmail.com

University of Kurdistan

Mohammad Darand

University of Kurdistan

Research Article

Keywords: actual evapotranspiration, complex network analysis, Granger causality, degree centrality, Eigenvector centrality.

Posted Date: August 24th, 2026

DOI: https://doi.org/10.21203/rs.3.rs-10301669/v1

License: This work is licensed under a Creative Commons Attribution 4.0 International License.
Read Full License

Additional Declarations: No competing interests reported.

Spatiotemporal Network Analysis of Actual Evapotranspiration Dynamics and Causal Teleconnections in Iran

Mohammad Kamangar[1*], Mohammad Darand[2]

[1]Postdoctoral Researcher in Climatology, Faculty of Natural Resources, University of Kurdistan, Sanandaj, Iran
Mohamad.kamangar63@gmail.com
[2]Professor of Climatology, Faculty of Natural Resources, University of Kurdistan, Sanandaj, Iran
m.darand@uok.ac.ir

Abstract

Long-term monitoring of actual evapotranspiration (ETa) is critical for assessing land–atmosphere water dynamics, yet optimizing monitoring networks requires a deeper understanding of spatial synchronization and predictive dependencies in water-limited environments. Utilizing GLEAM v4 satellite-derived data (1980–2023), we propose an integrated trend–topology–directionality framework to assess ETa variability across Iran. By combining long-term trend detection, complex network analysis, and Granger causality, this approach evaluates spatial connectivity to inform the design and optimization of regional environmental monitoring systems. Trend assessments (–0.03 to +0.13 mm/year) reveal rising ETa in the west/northwest and declines in the northeast, reflecting shifting hydroclimatic stress. Topological analysis of the spatial data exhibits a distinct core–periphery structure; high-degree centrality (0.001–0.43) in the central plateau (e.g., Dasht-e Kavir, Dasht-e Lut) indicates a highly synchronized core sensitive to large-scale atmospheric perturbations. Betweenness centrality metrics (≤0.03) highlight northeastern and central-eastern zones as critical spatial bridges, identifying priority locations for continuous monitoring stations. Furthermore, Granger causality isolates the northeast as a predictive source region influencing central/southeastern follower zones. Validated via spatial bootstrapping (correlation: 0.064–0.57), this framework provides a scientific basis for optimizing monitoring networks. By identifying predictive source regions and transitional nodes, the methodology provides a transferable template for environmental risk assessment and adaptive water resource management in similar large-scale, water-limited environments.

Keywords: actual evapotranspiration; complex network analysis; Granger causality; degree centrality; Eigenvector centrality.

Introduction

Evapotranspiration is a key component of the terrestrial hydrological cycle and plays a decisive role in the exchange of water and energy between the land surface and the atmosphere. However, recent studies indicate that accurately quantifying evapotranspiration across different spatial and temporal scales remains challenging. These challenges mainly arise from the lack of continuous data, the limited spatial coverage of ground-based measurements, and the insufficient understanding of the physical processes governing evapotranspiration, including the response to CO_2, plant stomatal regulation, soil evaporation, and the relationship between temperature and heat fluxes (Yi et al., 2024). These limitations have hindered the achievement of a reliable understanding of evapotranspiration variations and dynamics at regional and global scales.

The focus on actual evapotranspiration (ETa) is important because this variable directly reflects the real interactions among climatic conditions, soil moisture, and land surface cover. Studies have shown a significant divergence between trends in potential evapotranspiration (PET or ET_o) and ETa, particularly in water-limited regions where ETa is strongly controlled by precipitation and soil moisture (Anabalón and Sharma, 2017). It has also been reported that the widening gap between PET and ETa in some energy-limited and water-limited regions indicates the role of controlling variables beyond mere atmospheric demand (Vinukollu et al., 2011; Anabalón and Sharma, 2017). Therefore, ETa is considered a more realistic indicator for analyzing hydroclimatic changes compared with ET_0.

Previous studies have mainly focused on estimating ET through remote sensing products, physical models, and multi-model approaches. Despite the development of multi-source datasets, studies indicate that substantial uncertainties still exist in ET estimation, particularly in transition zones between arid and humid climates and in monsoonal regions (Vinukollu et al., 2011). Investigations also suggest that the spatial heterogeneity and persistence of ET pose a more critical challenge than temporal variations (Ezenne et al., 2023). In response to these limitations, some studies have emphasized analyzing long-term mean spatial patterns of ET and have demonstrated that evaluating hydrological model performance based on ET spatial patterns can mitigate the deficiencies of time-series-based approaches (Stisen et al., 2021). In addition, novel frameworks based on complex networks have been introduced for analyzing interactions among hydrological variables, enabling the investigation of spatial linkages and the identification of moisture bottlenecks (Mondal and Mishra, 2024). Despite these advances, important limitations remain in understanding the in a broad spatial context organization of ETa dynamics, particularly in arid and semi-arid environments. Most previous studies have primarily focused on estimation accuracy, remote sensing evaluation, uncertainty analysis, and long term trend detection (Vinukollu et al., 2011; Ezenne et al., 2023; Yi et al., 2024). Although these efforts have improved the understanding of evapotranspiration variability, ETa dynamics have largely been examined at pixel or basin scales rather than as components of interacting spatial systems. Consequently, the structure of spatial dependencies and regional interactions in ETa variability remains insufficiently explored.

At the same time, recent studies have highlighted the growing importance of network-based approaches for investigating large-scale hydrological interactions and hydroclimatic connectivity patterns (Donges et al., 2009; Mondal and Mishra, 2024). Nevertheless, the application of these frameworks to ETa dynamics remains limited, particularly at regional scales and in climate-stressed dryland environments. Consequently, important questions remain insufficiently explored, including whether ETa variability forms coherent spatial interaction networks, which regions exert stronger structural influence within these networks, and how directional predictive relationships propagate across hydroclimatically connected regions.

Addressing these gaps is particularly important for Iran, where pronounced climatic gradients, recurrent drought, uneven precipitation distribution, and severe water stress create highly heterogeneous hydroclimatic conditions. Although several studies have investigated evapotranspiration trends and spatial variability in Iran (Raziei and Pereira, 2013; Tabari et al., 2012; Pourmansouri et al., 2020), a comprehensive network-oriented assessment of ETa organization and directional dependency structures at the national scale remains largely unavailable.

This study presents an integrated framework for analyzing ETa dynamics by combining spatial correlation networks, centrality analysis, Granger based directional dependence, and bootstrap validation. Unlike conventional pixel based approaches, this framework examines ETa as a spatially connected system and identifies regions that play an important role in shaping broader patterns of variability. The framework is applied to long term GLEAM v4 data over Iran, which includes a wide range of hydroclimatic conditions, from hyper arid interior regions to humid coastal and mountainous areas. This diversity makes Iran a suitable setting for evaluating the performance of the framework across contrasting environmental conditions. Beyond its relevance to Iran, the proposed approach can also support ETa assessments in other regions with complex climatic and geographic settings.

Data and Methods

Study Area

Iran, located in southwestern Asia (25–40°N, 44–63°E), predominantly falls within arid and semi-arid climate zones (Alizadeh, 2009). The country's complex topography, particularly the Alborz and Zagros mountain ranges, generates highly variable precipitation patterns, resulting in humid regions along the Caspian Sea coasts and the Zagros foothills, while the central plateau and eastern deserts experience hyper-arid conditions (Fig. 1). The coastal areas along the Persian Gulf and the Gulf of Oman also exhibit high humidity and extreme temperatures, yet receive limited rainfall (Kamali et al., 2020; Namroodi et al., 2021). According to the Iranian Meteorological Organization's annual report (2022), the average ETa across the country is approximately 2.7 times the global mean, reaching up to five times the global average in desert and hyper-arid regions. Although minor discrepancies in reported rates may arise from differences in methodology, selected indices, or temporal data coverage, all reliable sources emphasize Iran's exceptionally

high evapotranspiration and its critical role in exacerbating water scarcity. This is particularly significant in Iran's arid and semi-arid regions, where ETa rates range between 2.7–5 times the global average. The country's steep climatic gradients—from the humid Caspian lowlands to hyper-arid deserts—combined with complex topography and variable precipitation, highlight the necessity of functional zoning based on Eta .

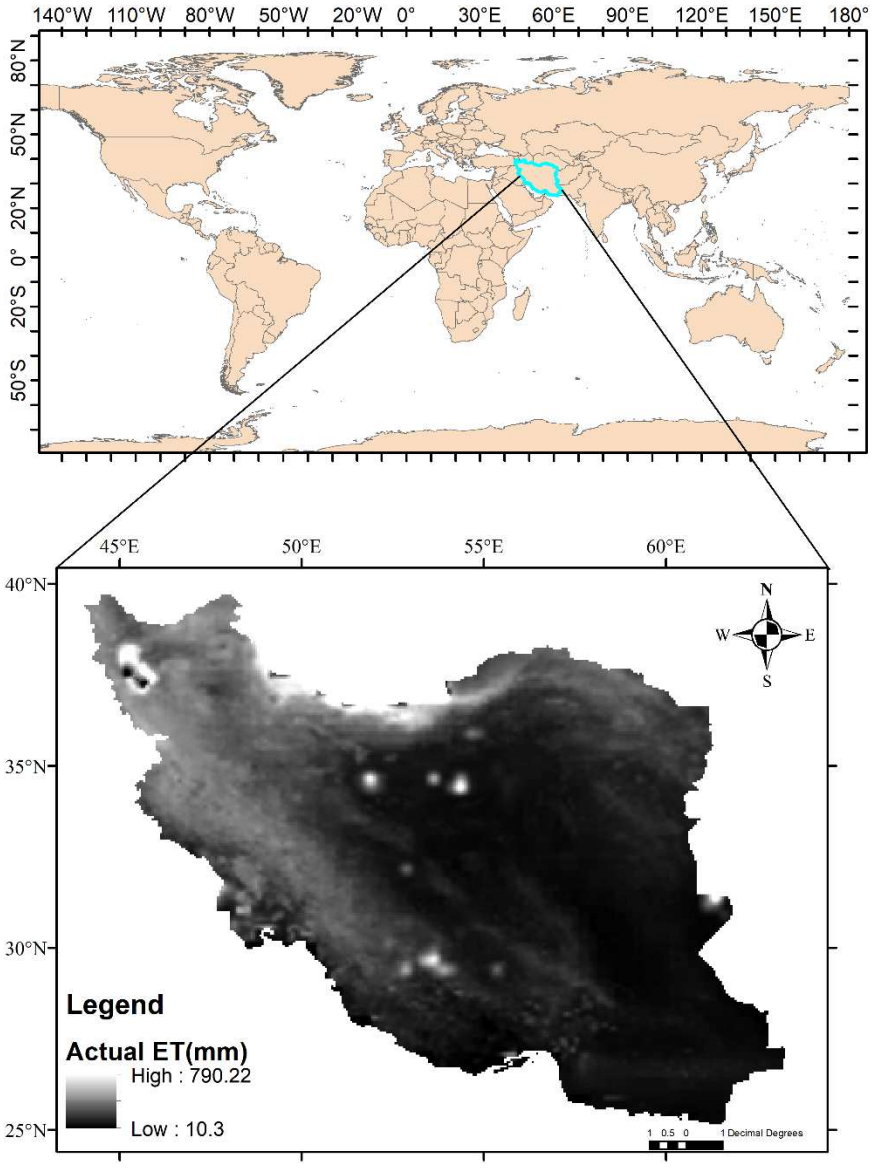


Fig 1. Spatial distribution of long-term mean annual ETa across Iran (mm yr⁻¹)

Data

In this study, we used GLEAM v4 as the main source of evapotranspiration data. This dataset provides annual ETa estimates from 1980 to 2023 at a spatial resolution of 0.1° over global land areas. The annual time scale was selected to reduce seasonal noise and emphasize long term variability in terrestrial water fluxes. GLEAM v4 combines physically based modeling with constraints from eddy covariance and sap flow observations, which improves the estimation of ETa and evaporative stress. The dataset also includes related variables such as transpiration, soil evaporation, interception loss, soil moisture, potential evapotranspiration, sensible heat flux, and evaporative stress. Previous studies have reported good agreement between GLEAM v4 and in situ observations, with median correlation coefficients ranging from 0.73 to 0.95, a Kling Gupta Efficiency of 0.49 across 473 global flux tower sites, and an RMSE of 0.95 mm day-1 (Miralles et al., 2025). It has also outperformed MOD16 and LSA SAF in several regional evaluations (Guo et al., 2022; Martens et al., 2018). Compared with version 3, the updated GLEAM v4 framework has reduced errors in evaporative stress estimates by about 15 to 20 percent (Miralles et al., 2025).

Analytical framework

To investigate the spatiotemporal organization of ETa across Iran, this study developed an integrated analytical framework that combines spatial correlation networks, graph-theoretic metrics, Granger causality analysis, and bootstrap-based validation. The approach was designed to identify dominant spatial interaction structures, distinguish influential and peripheral ETa pixels, and evaluate whether the inferred network relationships are temporally robust and statistically meaningful. The workflow consisted of five main stages:

1. Preparation of pixel-wise ETa time series and geographic coordinates;
2. Construction of a spatial ETa network based on pairwise temporal correlation;
3. Extraction of centrality-based network descriptors;
4. Identification of directional relationships using Granger causality; and
5. Validation through bootstrap resampling, null-model comparison, and time-split causality testing.

This framework draws conceptually on complex network analysis in geosciences and hydrology, where spatially distributed environmental variables are represented as nodes connected through

154 statistically significant similarity or dependency relationships (Tsonis and Roebber, 2004; Donges
155 et al., 2009; Boccaletti et al., 2006; Barabási, 2016).

156 The input dataset was organized in tabular form, where each row represented a spatial pixel and
157 the columns contained: longitude, latitude, and a sequence of ETa observations through time. ETa
158 data were obtained from the GLEAM v4 product for the period 1980–2023 at a spatial resolution
159 of 0.1°over Iran. The dataset was organized as a pixel-by-time matrix, as defined in Eq. (1):

160 $$\mathrm{X} = [x_{i,t}] \in \mathbb{R}^{N \times T}, \qquad (1)$$

161 where $x_{i,t}$denotes the ETa value of pixel $i$at time t, $N$is the total number of valid pixels, and $T$is
162 the number of annual observations. For the present study period, $T = 44$.

163 To remove the effect of differences in absolute ETa magnitude among pixels and emphasize
164 temporal co-variability, each pixel-wise time series was first mean-centered according to Eq. (2):

165 $$\tilde{x}_{i,t} = x_{i,t} - \bar{x}_i, \bar{x}_i = \frac{1}{T}\sum_{t=1}^{T} x_{i,t}\,, \qquad (2)$$

166 where $\bar{x}_i$is the temporal mean ETa of pixel i. The centered series was then normalized using Eq.
167 (3):

168 $$z_{i,t} = \frac{\tilde{x}_{i,t}}{\sqrt{\sum_{t=1}^{T} \tilde{x}_{i,t}^2 + \varepsilon}}, \varepsilon = 10^{-9}. \qquad (3)$$

169 As obtained from Eq. (3), each time series was transformed into a unit-length vector, thereby
170 allowing pairwise similarity estimates to reflect temporal behavior rather than absolute ETa values.

171 The similarity between pixels $i$and $j$was quantified using the Pearson correlation coefficient, which
172 was calculated from the normalized ETa series according to Eq. (4):

173 $$r_{ij} = \sum_{t=1}^{T} z_{i,t}\, z_{j,t}. \qquad (4)$$

174 By applying Eq. (4) to all pixel pairs, a symmetric correlation matrix was obtained, as expressed
175 in Eq. (5):

$$\mathrm{R} = [r_{ij}] \in \mathbb{R}^{N\times N}. \qquad (5)$$

The ETa interaction network was then constructed by thresholding the correlation matrix. Specifically, the adjacency matrix Awas derived from Eq. (6) using an absolute correlation threshold of $\tau = 0.70$:

$$a_{ij} = \begin{cases} 1, & \text{if } |\, r_{ij}\,| > 0.70 \text{ and } i \neq j, \\ 0, & \text{otherwise.} \end{cases} \qquad (6)$$

According to Eq. (6), two pixels were connected only when their temporal ETa association exceeded the selected threshold, while self-links were excluded by setting $a_{ii} = 0$. The threshold value of $|\tau|$ = 0.70 was selected to retain relatively strong positive or negative temporal dependencies while avoiding excessive network densification caused by weak correlations. Threshold-based correlation filtering is widely used in climate and hydroclimatic network studies to emphasize robust interaction structures and suppress potentially noisy or spurious links (Tsonis and Roebber, 2004; Donges et al., 2009). To evaluate the sensitivity of the resulting topology to threshold selection, additional networks were also constructed using $|\tau|$ = 0.60 and $|\tau|$ = 0.80. The major spatial connectivity patterns and dominant centrality structures remained qualitatively consistent across thresholds, indicating that the inferred ETa interaction architecture is reasonably robust to moderate threshold variations.

The structural role of each node in the ETa network was characterized using four standard centrality measures. Degree centrality was calculated according to Eq. (7):

$$C_D(i) = \frac{k_i}{N-1}, k_i = \sum_{j=1}^{N} a_{ij}\,, \qquad (7)$$

where k_i, as obtained from Eq. (7), represents the number of direct links connected to node i. Betweenness centrality was then computed from Eq. (8):

$$C_B(i) = \sum_{s\neq i\neq t} \frac{\sigma_{st}(i)}{\sigma_{st}}, \qquad (8)$$

where σ_{st}denotes the total number of shortest paths between nodes $s$and t, and $\sigma_{st}(i)$is the number of those paths passing through node i. Closeness centrality was derived according to Eq. (9):

$$C_C(i) = \frac{N-1}{\sum_{j \neq i} d(i,j)}, \qquad (9)$$

where $d(i,j)$is the shortest-path distance between nodes $i$and j. In addition, eigenvector centrality was obtained by solving the eigenvalue problem in Eq. (10):

$$\mathrm{Ac} = \lambda \mathrm{c}, \qquad (10)$$

where $\lambda$is the dominant eigenvalue and cis the corresponding eigenvector.

Based on the centrality measures obtained from Eqs. (7)– (10), each pixel was assigned a relative structural role within the ETa network. For descriptive interpretation, nodes with both degree and betweenness centrality above the 75th percentile were classified as structurally influential, whereas those with both metrics below the 25th percentile were classified as structurally peripheral. This categorization was intended to describe topological prominence only and was not interpreted as direct physical causality. Because the correlation network defined by Eq. (6) is undirected and therefore cannot represent directional dependence, pairwise Granger causality analysis was additionally applied to the annual ETa series. For each ordered pair of pixels (j, i), a bivariate autoregressive framework with a maximum lag of $p = 2$years was used. The restricted model is given in Eq. (11):

$$x_i(t) = \sum_{m=1}^{p} \alpha_m \, x_i(t-m) + \epsilon_t, \qquad (11)$$

whereas the unrestricted model is defined in Eq. (12):

$$x_i(t) = \sum_{m=1}^{p} \alpha_m \, x_i(t-m) + \sum_{m=1}^{p} \beta_m \, x_j(t-m) + \eta_t. \qquad (12)$$

The null hypothesis of no directional predictive influence was formulated according to Eq. (13):

$$H_0: \beta_1 = \beta_2 = \cdots = \beta_p = 0. \qquad (13)$$

Based on the comparison between Eqs. (11) and (12), a directed edge $j \rightarrow i$was retained when the corresponding F-test indicated statistical significance at $p < 0.05$. For each node, the number of outgoing and incoming significant causal links was then summarized as $G_{\text{out}}(i)$and $G_{\text{in}}(i)$, and the net directional score was obtained from Eq. (14):

$$G_{\text{net}}(i) = G_{\text{out}}(i) - G_{\text{in}}(i). \qquad (14)$$

As indicated by Eq. (14), positive values of $G_{\text{net}}(i)$correspond to relatively stronger source-like behavior, whereas negative values indicate relatively stronger receiver-like behavior. These values were subsequently normalized to the interval $[0, 1]$to enable integration with the bootstrap-derived stability metric. It should be noted that Granger causality does not imply direct physical causation; rather, it identifies statistically significant directional predictive dependencies between time series (Granger, 1969). Therefore, the inferred relationships in this study are interpreted as indicators of directional propagation structure and predictive influence within the ETa network rather than deterministic physical causality.

Bootstrap validation

To assess the robustness of the ETa network, a bootstrap resampling procedure with a sample size of B = 100 iterations was performed. In each iteration, pixels were resampled with replacement, the ETa matrix was re-normalized following Eqs. (2) and (3), and the network was reconstructed according to Eq. (6). The variability of node degree across bootstrap realizations was then quantified, and the degree-stability score was computed using Eq. (15):

$$S_D(i) = 1 - \frac{\sigma_k(i)}{\max(\sigma_k) + \varepsilon}. \qquad (15)$$

According to Eq. (15), larger values of $S_D(i)$, indicate greater topological stability, whereas lower values reflect stronger sensitivity to resampling.

To jointly evaluate structural persistence and directional prominence, a composite validation index was defined based on Eq. (16):

$$V(i) = 0.5\, S_D(i) + 0.5\, G_{\text{norm}}(i), \qquad (16)$$

where $G_{\mathrm{norm}}(i)$denotes the normalized directional score derived from Eq. (14). As obtained from Eq. (16), the validation index combines node-level stability and directional centrality with equal weights. In the present study, the resulting values ranged from 0.064 to 0.57, indicating substantial spatial heterogeneity in the robustness of ETa network nodes across Iran.Based on the values derived from Eq. (16), three broad classes of network validity were identified: high-validity nodes, intermediate-validity nodes, and low-validity nodes. These classes were used to interpret the spatial distribution of topological robustness and causal prominence at the national scale. To determine whether the network obtained from Eq. (6) departed from random organization, the observed ETa graph was compared with configuration-model null networks that preserve the empirical degree distribution while randomizing edge placement. In this step, network density and the clustering coefficient were compared against their null expectations.

In addition, the temporal persistence of the directional links derived from Eqs. (11)–(14) was examined by splitting the 44-year record into two equal sub-periods and repeating the Granger causality analysis independently for each half, using the same lag order ($p = 2$) and significance threshold ($p < 0.05$). A directional relationship was considered temporally robust only when it remained significant in both periods.

Results and Discussion

The spatiotemporal analysis of ETa across Iran shows that the trend slope during the study period varied between –0.03 and +0.13, indicating considerable spatial variability throughout the country. This pattern highlights the complex influence of climate, topography, vegetation cover, and precipitation on ETa dynamics. Areas with increasing ETa trends, shown in blue on the map, are mainly concentrated in western and northwestern Iran. The strongest positive trends were observed in Kurdistan, West Azerbaijan, East Azerbaijan, and parts of Zanjan and Hamadan, where slope values reached +0.13, indicating a significant increase in ETa over time. Additional scattered areas of increasing trends were also identified in Lorestan, Ilam, and parts of Chaharmahal and Bakhtiari, which may be related to local topographic and vegetation conditions. In contrast, negative ETa trends, illustrated by red to dark orange colors, were mainly found in northeastern Iran, particularly in Golestan and North Khorasan, where slope values decreased to –0.03. This indicates a gradual decline in ETa in these regions during the study period. Smaller areas with declining trends were also detected in some central and southern provinces, possibly reflecting local water limitations or microclimatic changes. Meanwhile, large parts of the Central Plateau, including Yazd, Kerman, and Semnan, as well as eastern provinces such as Sistan and Baluchestan and South Khorasan, showed near-zero slopes. These areas, represented by yellow to light orange tones, did not exhibit statistically significant temporal changes in ETa, suggesting that fluctuations remained limited and

largely within the range of natural year-to-year variability. Overall, the results reveal a clear spatially heterogeneous pattern of ETa change across Iran. Mountainous regions in the west, northwest, and parts of the south generally experienced increasing ETa, whereas the north and northeast showed notable declines. In contrast, the Central Plateau remained relatively stable (Fig. 2). These differences reflect Iran's strong climatic gradients, uneven precipitation distribution, varied topography, and diverse vegetation cover, and highlighting the importance of considering regional conditions when planning for water resources, agriculture, and ecosystem management.

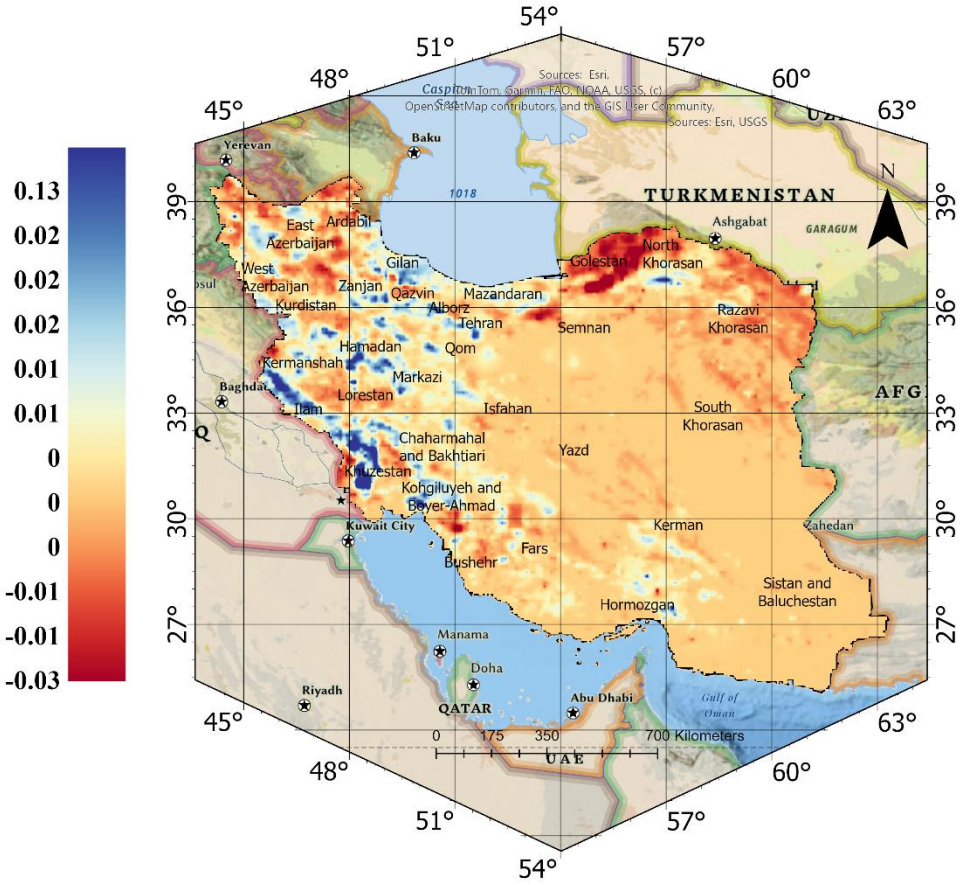


Fig 2. Spatial trends of ETa in Iran, showing increases in the west/northwest and decreases or stable values in the northeast and central plateau.

The spatial distribution of degree centrality in the ETa correlation network across Iran ranges from 0.001 to 0.43 (Fig. 3). The network is not uniform; instead, it exhibits a non-random spatial structure with clear clusters of high and low connectivity. High degree centrality values are concentrated in the central and eastern interior, including the Central Plateau, Dasht-e Kavir, Dasht-e Lut, and parts of eastern Isfahan, Yazd, Kerman, South Khorasan, and Sistan and Baluchestan. These areas form dense hubs where ETa fluctuations are strongly linked across large spatial extents.

Conversely, low degree centrality values are observed in the northern regions, parts of the central area near Namak Lake, and the southwest and southern coastal belts. This includes the Caspian littoral, the Alborz and Zagros highlands, and the Persian Gulf and Oman Sea coasts (Hormozgan and Bushehr). In these regions, degree centrality is lower, indicating a more fragmented pattern of connectivity between pixels compared to the interior drylands. From a network topology perspective, the degree centrality values follow a spatial gradient that mirrors Iran's aridity patterns, with higher connectivity in the central/eastern zones and lower connectivity in the mountainous and humid peripheries. The high-degree hubs function primarily as local clusters of synchronous ETa behavior rather than bridging nodes between different regions of the country. This results in a core-periphery structure, where the arid central core maintains strong internal connectivity, while the more humid northern, western, and southern peripheries display weaker and more heterogeneous link patterns.

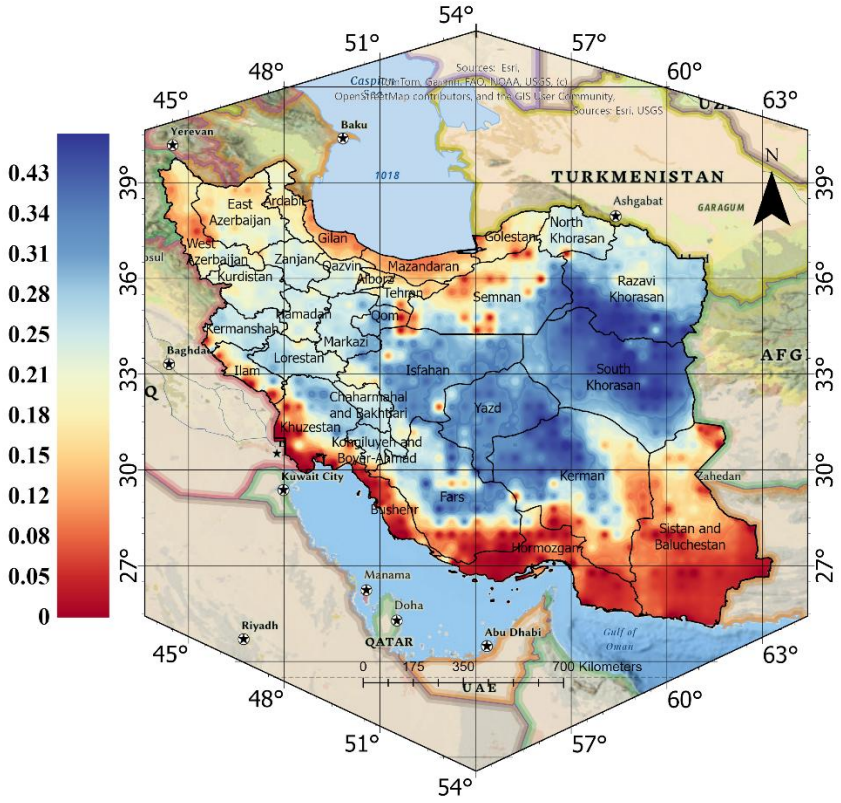


Fig3. Spatial distribution of Degree Centrality in Iran's ETa correlation network, highlighting highly connected hubs in the central and eastern dry regions and lower connectivity in the northern and western areas.

The spatial distribution of betweenness centrality reveals significant heterogeneity in connectivity across Iran's ETa network (Fig. 4). Betweenness values range from nearly 0 to 0.03, highlighting a stark contrast between nodal roles in the network. High betweenness centrality values (approaching 0.03) are primarily concentrated in the eastern and east-central parts of Iran. Notable

clusters are located in Khorasan Razavi, South Khorasan, southern Kerman, and sections of the Fars and Khuzestan provinces, as well as the Kohgiluyeh and Boyer-Ahmad mountains. These regions act as the primary bridges or bottlenecks within the network, connecting distinct ETa clusters across the country. In contrast, low betweenness centrality values—often near zero—cover large portions of the network. This includes northwestern Iran (Eastern and Western Azerbaijan, Kurdistan, Kermanshah, and Ilam), parts of the central plateau, the Caspian coastal provinces (Guilan and Mazandaran), the southern coastal strips, and southeastern Iran (Sistan and Baluchestan). In these regions, pixels exhibit minimal role in interregional connectivity, as ETa dynamics are characterized by more localized patterns rather than broad network linkages.

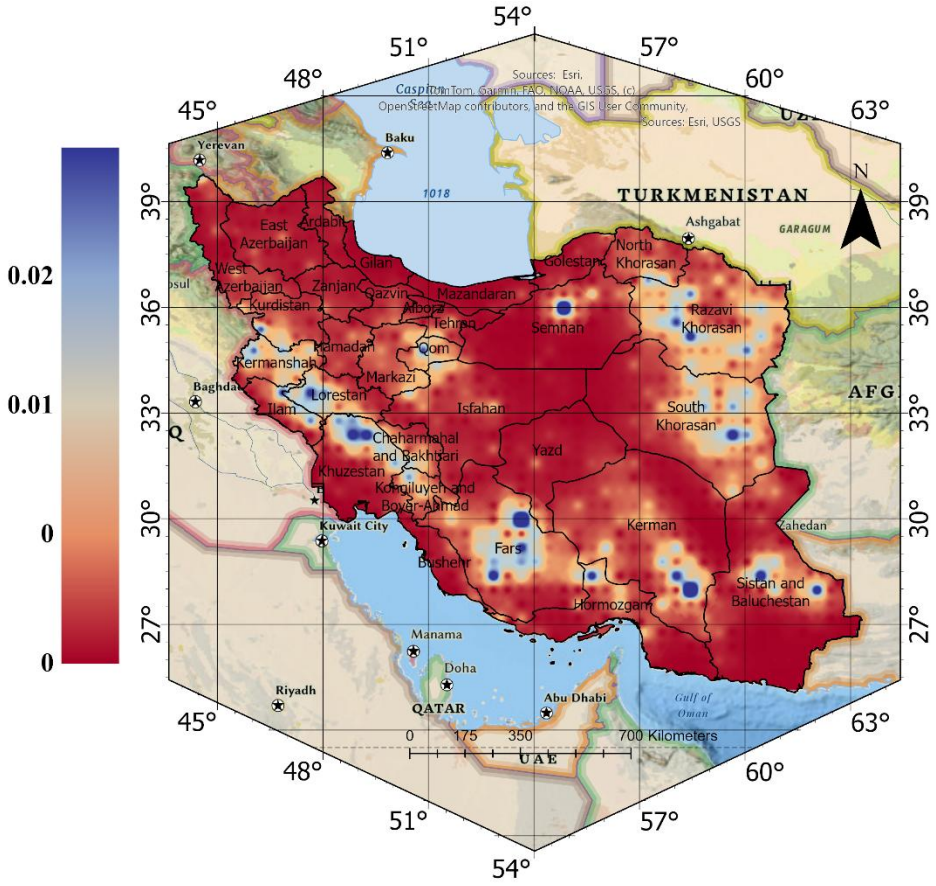


Fig. 4. Spatial distribution of betweenness centrality in Iran's ETa network.

The spatial distribution of closeness centrality in the ETa network shows a clear gradient, with values ranging from near 0 to 0.53 (Fig. 5). The highest closeness values, typically exceeding 0.44 (dark blue clusters), are concentrated across central and eastern Iran, including the Central Plateau, the Dasht-e Kavir and Lut deserts, and the eastern provinces of Razavi Khorasan, South Khorasan, and Yazd. High values also extend into the southern Zagros margins and parts of Isfahan and Kerman. These elevated values indicate that ETa fluctuations in the central core can propagate more efficiently to the rest of the network due to shorter correlation paths. In contrast, the lowest closeness centrality values (below 0.20, shown in red and orange) are predominantly located in the

northern and northwestern peripheries, including the Azerbaijan provinces, Kurdistan, and the Caspian littoral (Guilan and Mazandaran). Similarly, low values are observed in the southeastern corner, specifically in parts of Sistan and Baluchestan and along the Makran coast. The lower values in these regions suggest that ETa anomalies are more isolated and require longer or more complex correlation paths to interact with the broader national network. The spatial organization of closeness centrality follows a core-periphery pattern, declining from the central interior toward the northern, western, and southeastern margins. While betweenness centrality identifies specific bridging bottlenecks, the closeness centrality map highlights the central arid and semi-arid interior as the functional core of the network, characterized by high connectivity and rapid signal diffusion.

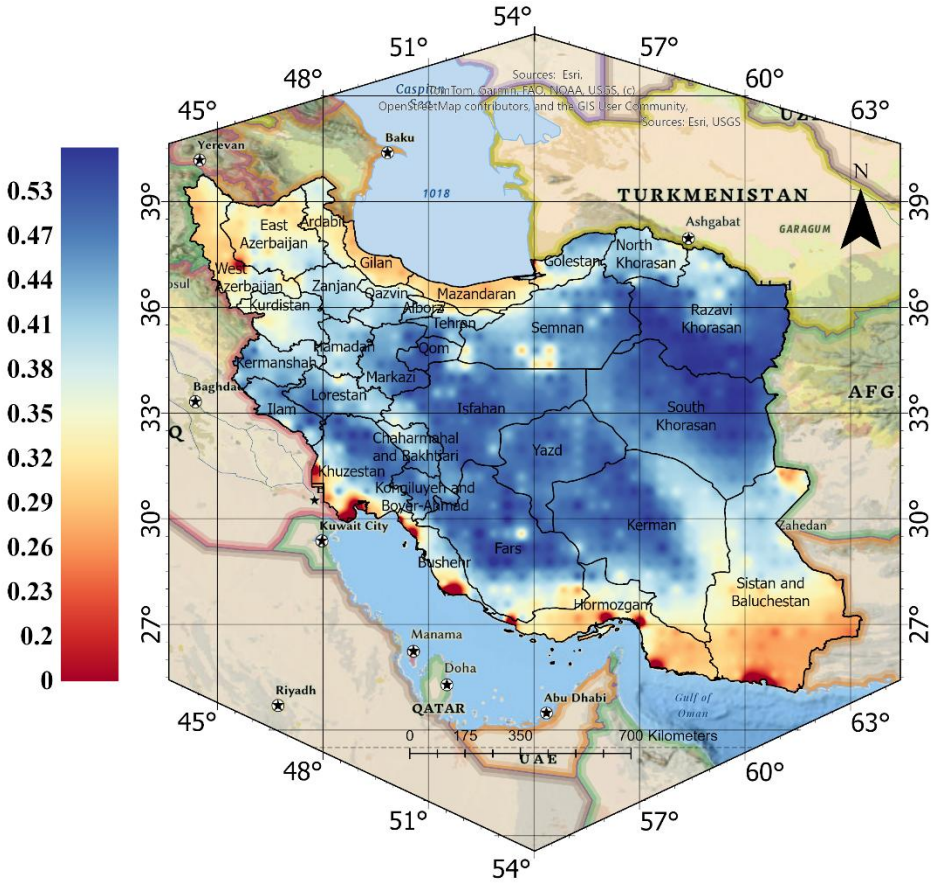


Fig. 5. Spatial distribution of closeness centrality in Iran's ETa network .

Spatial distribution of Granger centrality in the ETa network as the difference between the output and input causal links shows that the Granger centrality values range from 0.01 to 0.99, all of which are positive, with a color gradient from dark red (low values ~0.01) to dark blue (high values ~0.99) and most pixels are shown in light gray/green (medium values ~0.44–0.59). Strong drivers (dark blue, GC ~0.7–0.99) are mainly concentrated in northeastern Iran (Khorasan Razavi and Shomali) with scattered patches in Fars and central regions, acting as regions with stronger directional predictive influence where ETa changes strongly predict changes in other locations in the network. The follower/highly influenced regions (red/orange, GC ~0.01–0.34) are

concentrated in South Khorasan, Kerman, Yazd, and parts of Fars, which have low predictive power and are largely influenced by other nodes. The intermediate/mediator regions (gray/light green, GC ~0.39–0.64) cover most of western, northwestern, and southwestern Iran and large areas of the center and act neither as strong drivers nor as pure followers, but rather as transmitters or moderators in the directional dependency structure (Fig. 6). The directional causality pattern indicates a dominant flow from the northeast to the center, south, and southeast of Iran, with ETa fluctuations in the northeastern drivers predicting changes in the central and eastern dry regions of the follower, reflecting intra-country teleconnections in the Iranian hydrological cycle. Hydrological implications include that the northeastern regions act as early warning points for ETa changes in the central and eastern drylands, the central-eastern and southeastern follower regions are highly sensitive to driving disturbances with potentially rapid impacts on the water balance, and the midwestern/northwestern GC regions are less integrated into a strong directional dependency structure, indicating the dominance of local processes and relative independence. Unlike other network measures such as betweenness centrality that highlight bridging roles, Granger centrality demonstrates directional and predictive power, highlighting northeastern Iran as the main region exhibiting stronger predictive influence in the ETa network. These directional relationships should be interpreted as statistical predictive dependencies rather than deterministic physical causality.

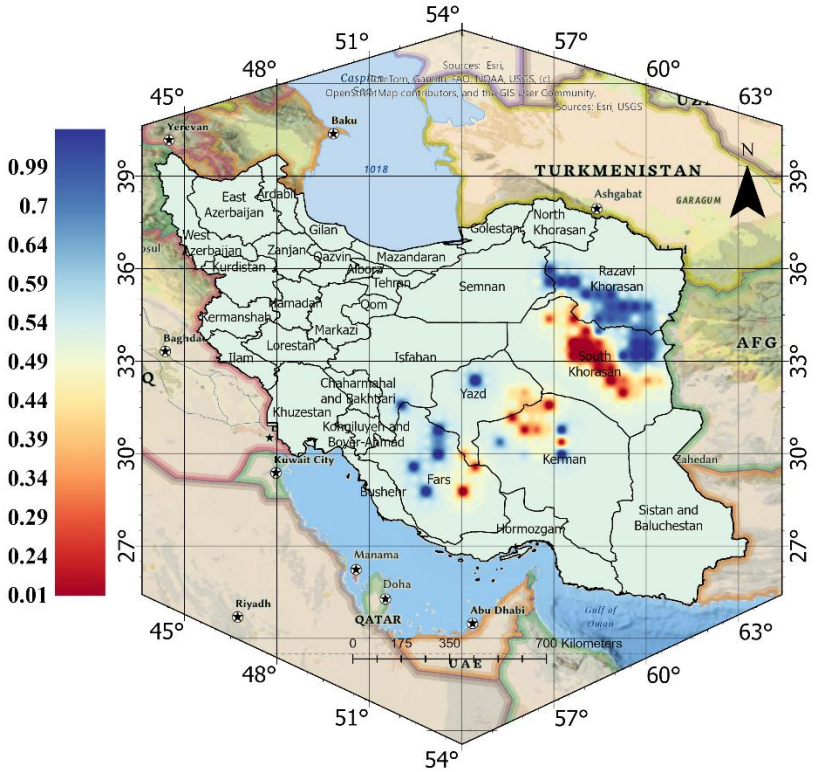


Fig. 6. Spatial distribution of Granger Centrality in Iran's ETa network, highlighting northeastern regions as key drivers influencing central and southeastern areas, while central-western and southern regions act as followers or neutral zones.

The spatial pattern of eigenvector centrality in the Iranian ETa correlation network exhibits a a distinct spatial structure, with values ranging from 0 to 0.067 (Fig. 7). High centrality values between 0.05 and 0.067 form a broad and spatially coherent core across central and eastern Iran. This core encompasses the Central Plateau, the Dasht e Kavir, the Dasht e Lut, and extensive areas of Yazd, South Khorasan, Kerman, and western Sistan and Baluchestan. The highest values are concentrated within the hyper arid interior basins, particularly the southern Dasht e Kavir and northern Dasht e Lut, where centrality approaches the upper bound of the distribution. Surrounding this core, moderately high values between approximately 0.03 and 0.05 extend into eastern Isfahan, northern Fars, Semnan, and parts of Markazi, forming a transitional belt rather than isolated clusters. In contrast, the lowest eigenvector centrality values below 0.01 are confined to peripheral regions in the northwest and southeast. In the northwest, very low values dominate West and East Azerbaijan, Ardabil, much of Kurdistan, and northern sectors of Zanjan and Gilan. These areas correspond to the complex topography of the Alborz and Zagros headwaters and the Caspian coastal zone. A comparable low centrality domain is observed in southern Sistan and Baluchestan, the Makran coastal plain, and eastern Hormozgan, where values remain close to zero. A smaller zone of reduced centrality is also present over the central Zagros highlands, including Chaharmahal and Bakhtiari and adjacent parts of Khuzestan. Between the central high value core and the peripheral low value domains, eigenvector centrality declines along distinct spatial gradients. The transition is particularly sharp along the northern margin of the Central Plateau, where values decrease rapidly toward the southern Caspian drainage divide. A more gradual gradient characterizes the southeastern transition from the Makran coast toward the Lut interior. Across the western Zagros arc, values generally fall within an intermediate range between 0.01 and 0.03, indicating neither core dominance nor marginal isolation. Northeastern provinces, including Razavi and North Khorasan, display moderate centrality levels that contrast with the persistently low values in the northwest. Isolated pockets of locally elevated centrality are detectable in the Bushehr coastal plain and the Jazmurian basin, suggesting secondary zones of network influence outside the principal interior core.

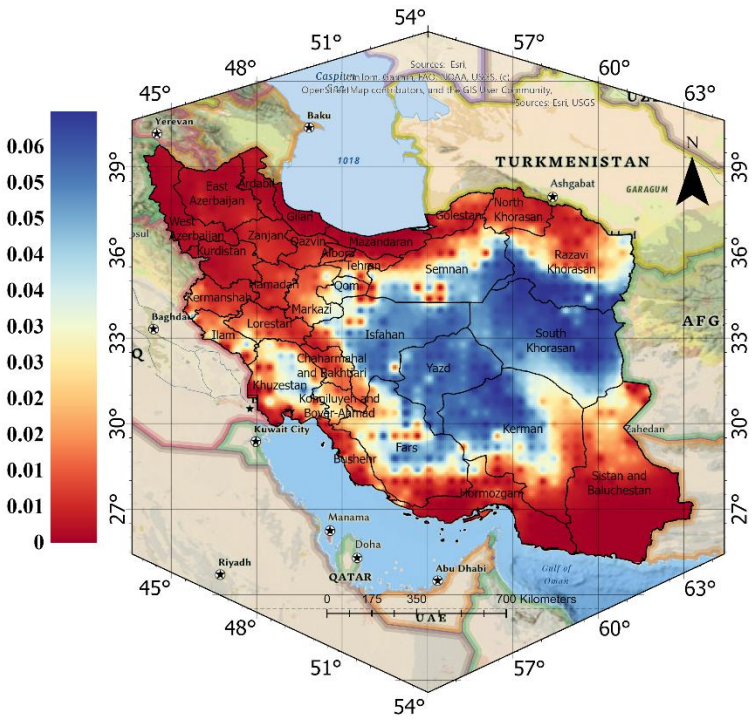


Fig 7. Eigenvector centrality of the ETa correlation network, High centrality dominates central/eastern Iran; low values cluster in the northwest and southeast.

Validation

The composite validation map reveals marked spatial variation in the robustness of the ETa network across Iran. Values range from 0.064 to 0.57, indicating that network stability is not spatially uniform (Fig. 8). Because this metric combines node degree stability from spatial bootstrapping with normalized Granger causal centrality, higher values identify areas where network topology remains persistent and directional interactions are more consistently supported. The map therefore reflects the reliability of the inferred network structure rather than simple association strength. The highest values occur in eastern and southern Khorasan, with smaller clusters in northern Yazd and parts of Fars Province. The spatial coherence of these zones suggests that ETa interactions are organized around stable and spatially consistent controls. In such regions, connectivity patterns remain largely preserved under resampling, which points to robust structural roles within the national network. These areas can therefore be interpreted as regions where both topological persistence and causal influence are comparatively strong. Intermediate values dominate much of the central plateau and extend into parts of northern and southern Iran. This pattern indicates moderate structural stability, where network relationships are present but less consistently reproduced across bootstrap realizations. The broad distribution of these values suggests transitional zones in which ETa dynamics are shaped by a mixture of climatic, topographic, and land surface factors rather than by a single dominant control. These regions contribute to national connectivity, but they do not appear to function as core structural anchors.

The lowest values are limited to scattered areas in central South Khorasan and parts of Fars Province. Here, the network structure is less stable, with weaker reproducibility of node connectivity and greater sensitivity of causal links to sampling variation. Their fragmented spatial pattern suggests localized instability rather than a widespread structural weakness. This behavior is likely associated with stronger surface heterogeneity or with ETa responses driven by short term and local scale processes. At the national scale, the map suggests a broad spatial organization in network stability, with more pronounced extremes in arid and semi-arid regions and more moderate values across much of the interior mountainous belt. This pattern indicates that ETa network coherence is closely tied to hydroclimatic regime and regional environmental homogeneity. Overall, the results show that the ETa network over Iran is spatially structured, with some regions contributing more strongly than others to the persistence and integrity of the national scale system.

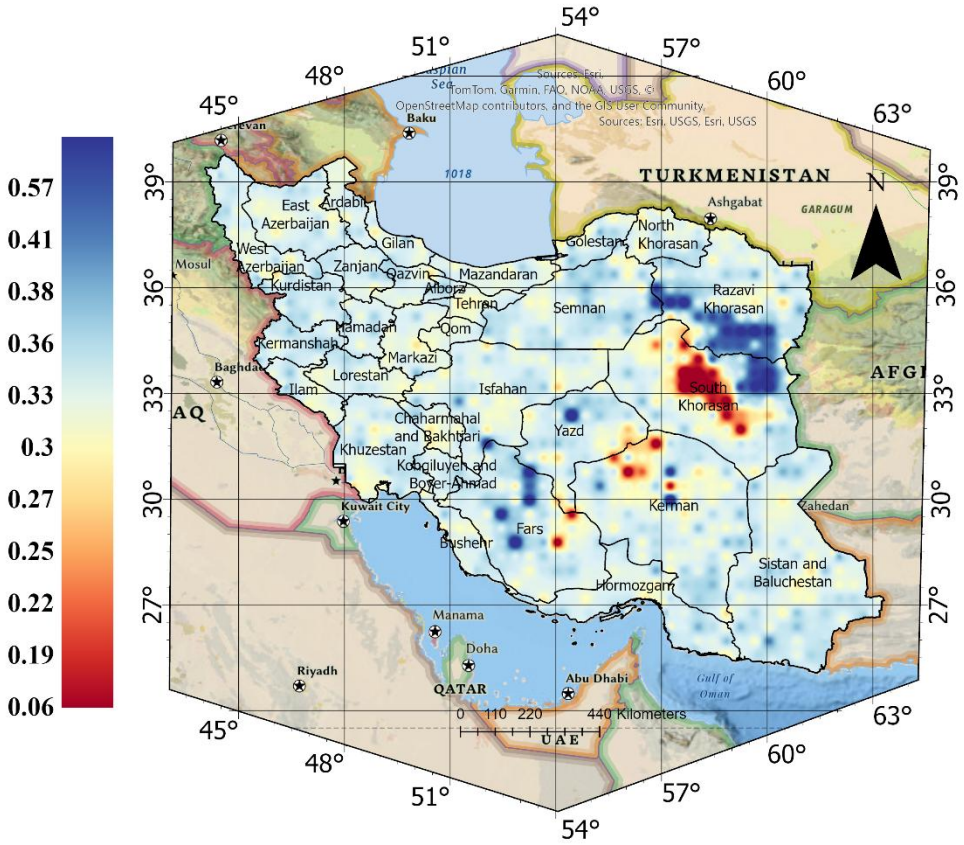


Fig. 8. Iran's ETa network Validation is denser and more clustered than random networks

The spatial organization and causal structure of ETa revealed in this study align with known macro-scale climate gradients in Iran, while providing a novel network-centric perspective on hydroclimatic connectivity. Traditional assessments of reference evapotranspiration (ETo) have consistently documented a sharp gradient transitioning from the humid Caspian littoral and mountainous northwest to the hyper-arid central plateau and southeastern basins (Zareabayneh et

al., 2011; Tabari et al., 2012; Raziei and Pereira, 2013). Our network analysis captures a complementary spatial structure, wherein the arid and semi-arid interior emerges as a highly integrated core characterized by elevated Degree, Eigenvector, and Closeness centralities. The high Closeness centrality values (exceeding 0.44) observed across the Central Plateau, Dasht-e Kavir, and Lut deserts point to a highly synchronized ETa regime in these water-limited environments. In these hyper-arid zones, ETa variability is strongly governed by regional atmospheric demand and severe moisture limitations rather than localized land-cover dynamics. This environmental homogeneity across dry zones, previously noted by Delghandi et al. (2017), facilitates the rapid propagation of ETa anomalies across long distances, effectively turning the interior into a coherent functional core. Conversely, the lower Closeness values (below 0.20) in the humid north and topographically complex northwest indicate more fragmented, localized ETa dynamics. In these energy-limited or transitional regimes, complex topography and heterogeneous vegetation cover disrupt broad-scale synchronization, leading to isolated behaviors and longer correlation paths to the rest of the network. This spatial heterogeneity is further refined by the distribution of Betweenness centrality, which highlights critical transmission pathways. While the central plateau forms the highly connected core, the eastern and east-central sectors, including South Khorasan, southern Kerman, and parts of Fars, act as structural bottlenecks with high Betweenness values. These regions serve as topological bridges connecting distinct regional ETa clusters. The existence of such routing hubs is consistent with the bottleneck structures identified in global evapotranspiration networks (Mondal and Mishra, 2024). Identifying these predictive and transmission hubs via Granger causality aligns with broader hydroclimatic applications of causal discovery (Ombadi et al., 2020; Yu et al., 2025). Such Granger-based causal structures find strong methodological support in established causal frameworks like TETRAD and PCMCI (Ramsey et al., 2018; Schilling et al., 2026), which emphasize the validity of autoregressive causal detection in gridded climate fields. Under stress conditions, these highly central regions can amplify hydroclimatic perturbations. This phenomenon parallels findings by Gupta and Jain (2021), who demonstrated that evapotranspiration-linked drought indices (such as SPEI) show enhanced sensitivity to large-scale teleconnections compared to precipitation-based metrics due to non-linear land-atmosphere feedbacks.

The temporal dynamics of the network also show partial agreement with documented regional trends. The positive ETa trends observed in western and northwestern Iran correspond with rising temperature and evaporative demand trends reported by Nouri et al. (2018), Dinpashoh et al. (2019), and Pourmansouri et al. (2020). However, the weak or negative ETa trends in parts of the northeast diverge from ETo-based projections. This divergence underscores the physical distinction between potential evaporative demand (ETo) and actual, soil-moisture-constrained water loss (ETa), particularly in degrading drylands where water limitation prevents ETa from keeping pace with rising atmospheric demand.

Finally, the composite validation score provides an independent spatial evaluation of these network patterns. The higher validation stability observed in the humid northwest and northern sectors is

consistent with previous product evaluations in Iran, which show that satellite and model-based ET datasets perform more reliably in climatologically stable and water-abundant regions (Rahimpour et al., 2018; Moshir Panahi et al., 2021). The lower validation scores in the arid interior, despite its high network centrality, highlight a critical challenge: the very regions that dictate the network's topological connectivity are also those associated with the highest estimation uncertainties. Consequently, while the macro-scale gradients of ETa are compatible with classical climatological divisions, this network-based framework reveals a deeper, structurally interconnected system where localized dryland dynamics exert a disproportionate influence on the national-scale evapotranspiration field.

While GLEAM v4 offers a consistent long-term record, its 0.25°spatial resolution inevitably averages out sub-grid hydrological processes across complex terrains like the Alborz and Zagros mountains. Integrating higher-resolution satellite observations or blending global products with local gauge networks would better resolve these high-elevation pathways. Furthermore, the current network primarily captures climate-driven ETa patterns, omitting intensive anthropogenic influences such as dam regulations and groundwater-based irrigation. Disentangling these human signatures from natural hydroclimatic connectivity remains an essential step toward representing real-world water dynamics.

Methodologically, relying on Granger causality and linear correlation might underrepresent rapid, non-linear hydroclimatic shocks, including flash droughts or extreme heatwaves. Transitioning to non-linear causal discovery tools, such as transfer entropy or constraint-based algorithms, could better capture these sudden transitions. Finally, while Iran serves as an excellent testbed due to its environmental heterogeneity, testing this framework across other data-scarce arid regions globally will confirm its scalability and refine its utility as a transferable tool for regional water resource monitoring.

Conclusion

This study shows that the spatial behavior of ETa in Iran cannot be understood adequately through trend maps alone. Although long-term changes are important, the broader picture only becomes clear when temporal trends are examined together with network structure and directional dependence. Viewed in this way, ETa over Iran forms an organized spatial system in which some regions are structurally central, some act as bridges, and others exert stronger predictive influence over downstream areas. The trend analysis revealed a heterogeneous pattern across the country. Increasing ETa was concentrated mainly in western and northwestern Iran, whereas declining trends were more evident in the northeast. By contrast, much of the Central Plateau showed little long-term change. Yet this apparent stability did not correspond to marginal importance in the network. Degree, closeness, and eigenvector centrality consistently indicate that the central and eastern interior—particularly the Central Plateau, Dasht-e Kavir, and Dasht-e Lut—constitutes the main topological core of the ETa network. These dryland regions are not the most rapidly changing

in trend terms, but they are the most internally synchronized and structurally central within the national correlation pattern. A different picture emerges from the directional analysis. Granger causality identifies northeastern Iran as the main predictive source region, with influence extending toward central, southern, and southeastern follower zones. This distinction is essential for interpretation. The topological core of the network is centered in the arid interior, whereas the strongest directional drivers are concentrated in the northeast. In other words, structural centrality and predictive control are related, but they are not geographically identical. This distinction has practical significance. Monitoring strategies should not focus only on areas with the strongest trends, but also on regions that occupy key structural and predictive positions within the national ETa system. Prioritizing central core areas, bridging zones, and northeastern source regions could improve the efficiency of environmental monitoring and strengthen early warning capacity in water-limited landscapes. More broadly, the framework developed here provides a robust basis for understanding hydrological connectivity and for supporting adaptive water-resource planning under increasing climatic pressure.

Declaration of generative AI and AI-assisted technologies in the writing process: During the preparation of this work, the author s used generative AI in order to improve language and readability. After using this tool/service, the authors reviewed and edited the content as needed and take(s) full responsibility for the content of the publication.

CRediT authorship contribution statement

Mohammad Kamangar: conceptualized, curated, and analyzed the data, formal analysis, and writing original draft. **Mohammad Darand**: developed the methodology, project administration, validated the results, edited the manuscript, and supervision.

Declaration of competing interest

The authors declare that they have no known competing financial interests or personal relationships that could have appeared to influence the work reported in this paper.

Acknowledgements

The authors gratefully acknowledge the GLEAM v4 team for providing the long-term ET_a dataset and the Köppen–Geiger climate classification (Beck et al., 2023) for comparative analyses. We also thank the developers of the Python open-source ecosystem (TensorFlow, Scikit-learn, GeoPandas, and Matplotlib) that supported the modeling and visualization workflows.

Funding

Financial support was provided by the Vice President for Research and Innovation, University of Kurdistan, post-doctoral contract number ص/3/9/22599.

Reference

Alizadeh, A. (2009). Principles of applied hydrology (In Persian). Mashhad: Imam Reza University Press.

Anabalón, A., & Sharma, A. (2017). On the divergence of potential and actual evapotranspiration trends: An assessment across alternate global datasets. *Earth's Future*, *5*(9), 905-917.

Barabási, A.-L. (2016). *Network Science*. Cambridge University Press.

Boccaletti, S., Latora, V., Moreno, Y., Chavez, M., & Hwang, D.-U. (2006). Complex networks: Structure and dynamics. *Physics Reports*, 424(4–5), 175–308.

Calixto, K. G., Coutinho, J. V., & Wendland, E. (2021). Causality and Time-Lagged Dependencies at the Watershed Scale.

Delghandi, M., Joorabloo, S., & Emamgholizadeh, S. (2017). Climate change impacts on spatial-temporal variations of reference evapotranspiration in Iran. *Water Harvesting Research*, *2*(1), 13-23.

Dinpashoh, Y., Jahanbakhsh-Asl, S., Rasouli, A. A., Foroughi, M., & Singh, V. P. (2019). Impact of climate change on potential evapotranspiration (case study: west and NW of Iran). *Theoretical and Applied Climatology*, *136*(1), 185-201.

Donges, J. F., Zou, Y., Marwan, N., & Kurths, J. (2009). Complex networks in climate dynamics. *The European Physical Journal Special Topics*, 174, 157–179.

Ezenne, G. I., Eyibio, N. U., Tanner, J. L., Asoiro, F. U., & Obalum, S. E. (2023). An overview of uncertainties in evapotranspiration estimation techniques. *Journal of Agrometeorology*, *25*(1), 173-182.

Granger, C. W. J. (1969). Investigating causal relations by econometric models and cross-spectral methods. *Econometrica*, 37(3), 424–438.

Guo, X., Meng, D., Chen, X., & Li, X. (2022). Validation and comparison of seven land surface evapotranspiration products in the Haihe River Basin, China. Remote Sensing, 14(17), 4308.

Gupta, V., & Jain, M. K. (2021). Unravelling the teleconnections between ENSO and dry/wet conditions over India using nonlinear Granger causality. *Atmospheric Research*, *247*, 105168.

Kamali, A., Khosravi, M., & Hamidianpour, M. (2020). Spatial–temporal analysis of net primary production (NPP) and its relationship with climatic factors in Iran. Environmental Monitoring and Assessment, 192, 718. https://doi.org/10.1007/s10661-020-08667-7

Kamali, M. I., Nazari, R., Faridhosseini, A., Ansari, H., & Eslamian, S. (2015). The determination of reference evapotranspiration for spatial distribution mapping using geostatistics. *Water Resources Management*, *29*(11), 3929-3940.

Martens, B., de Jeu, R., Verhoest, N., Schuurmans, H., Kleijer, J., & Miralles, D. G. (2018). Towards estimating land evaporation at field scales using GLEAM. Remote Sensing, 10, 1720.

Miralles, D. G., Bonte, O., Koppa, A., Baez-Villanueva, O. M., Tronquo, E., Zhong, F., ... & Haghdoost, S. (2025). GLEAM4: global land evaporation and soil moisture dataset at 0.1 resolution from 1980 to near present. *Scientific data*, *12*(1), 416.

Mondal, S., & Mishra, A. (2024). Quantifying the precipitation, evapotranspiration, and soil moisture network's interaction over global land surface hydrological cycle. *Water Resources Research*, *60*(2), e2023WR034861.

Mondal, S., & Mishra, A. K. (2025). A complex network-based framework for evaluating hydrometric monitoring networks. *Stochastic Environmental Research and Risk Assessment*, *39*(9), 3979-3993.

Moshir Panahi, D., Sadeghi Tabas, S., Kalantari, Z., Ferreira, C. S. S., & Zahabiyoun, B. (2021). Spatio-temporal assessment of global gridded evapotranspiration datasets across Iran. *Remote Sensing*, *13*(9), 1816.

Namroodi, M., Hamidianpour, M., & Poodineh, M. (2021). Spatio-temporal analysis of changes in heat and cold waves across Iran over the statistical period 1966–2018. Arabian Journal of Geosciences, 14, 857. https://doi.org/10.1007/s12517-021-07161-9

Newman, M. (2010). *Networks: An Introduction*. Oxford University Press.

Nouri, M., Homaee, M., & Bannayan, M. (2018). Spatiotemporal reference evapotranspiration changes in humid and semi-arid regions of Iran: past trends and future projections. *Theoretical and Applied Climatology*, *133*(1), 361-375.

Ombadi, M., Nguyen, P., Sorooshian, S., & Hsu, K. L. (2020). Evaluation of methods for causal discovery in hydrometeorological systems. *Water Resources Research*, *56*(7), e2020WR027251.

Pourmansouri, F., & Rahimzadegan, M. (2020). Evaluation of vegetation and evapotranspiration changes in Iran using satellite data and ground measurements. *Journal of Applied Remote Sensing*, *14*(3), 034530-034530.

Rahimpour, M., Karimi, N., Rouzbahani, R., & Eftekhari, M. (2018). Validation and calibration of FAO WaPOR product (actual evapotranspiration) in Iran using in-situ measurements. *Iran-Water Resources Research*, *14*(2), 254-263.

Ramsey, J. D., Zhang, K., Glymour, M., Romero, R. S., Huang, B., Ebert-Uphoff, I., ... & Glymour, C. (2018, September). Tetrad—a toolbox for causal discovery. In *8th international workshop on climate informatics* (pp. 1-4). Boulder Colorado: National Center for Atmospheric Research.

Raziei, T., & Pereira, L. S. (2013). Spatial variability analysis of reference evapotranspiration in Iran utilizing fine resolution gridded datasets. *Agricultural Water Management*, *126*, 104-118.

627 Schilling, S., Bolch, T., Dietz, A., Herman, R. J., & Kuenzer, C. (2026). Snowmelt Influence on Northern
628 Hemisphere River Discharge–The Potential of Causal Inference for Assessing Long-Term
629 Trends. *EGUsphere*, *2026*, 1-48.

630 Siabi, N., Sanaeinejad, S. H., & Ghahraman, B. (2022). Effective method for filling gaps in time series of
631 environmental remote sensing data: An example on evapotranspiration and land surface temperature
632 images. *Computers and Electronics in Agriculture*, *193*, 106619.

633 Stisen, S., Soltani, M., Mendiguren, G., Langkilde, H., Garcia, M., & Koch, J. (2021). Spatial patterns in
634 actual evapotranspiration climatologies for europe. *Remote Sensing*, *13*(12), 2410.

635 Tabari, H., Aeini, A., Talaee, P. H., & Some'e, B. S. (2012). Spatial distribution and temporal variation of
636 reference evapotranspiration in arid and semi-arid regions of Iran. *Hydrological Processes*, *26*(4), 500-512.

637 Tsonis, A. A., & Roebber, P. J. (2004). The architecture of the climate network. *Physica A*, 333, 497–504.

638 Tsonis, A. A., & Swanson, K. L. (2008). Topology and predictability of El Niño and La Niña networks.
639 *Physical Review Letters*, 100, 228502.

640 Vinukollu, R. K., Meynadier, R., Sheffield, J., & Wood, E. F. (2011). Multi-model, multi-sensor estimates of
641 global evapotranspiration: Climatology, uncertainties and trends. *Hydrological Processes*, *25*(26), 3993-
642 4010.

643 Yang, X. (2023). *Complex Hydroclimate System Modeling: Causation, Tipping, and Extremes* (Doctoral
644 dissertation, Arizona State University).

645 Yi, K., Senay, G. B., Fisher, J. B., Wang, L., Suvočarev, K., Chu, H., ... & Baldocchi, D. (2024). Challenges
646 and future directions in quantifying terrestrial evapotranspiration. *Water Resources Research*, *60*(10),
647 e2024WR037622.

648 Yu, J., Zhang, Y., Liang, H., Liu, H., Liu, J., Mello, C. R., ... & Guo, L. (2025). A dual-method, multi-scale
649 causal framework reveals seasonal shifts in hydrological causality of a headwater catchment. *Journal of*
650 *Hydrology*, 134891.

651 Zareabayneh, H., Bayat Varkeshi, M., Sabziparvar, A. A., Marofi, S., & Ghasemi, A. (2011). Evaluation of
652 different reference evapotranspiration methods and their zonings in Iran. *Physical Geography*
653 *Research*, *42*(4), 95-109.

654